An Ultra-High-Speed, 500000 rpm, 1 kW Electrical Drive System

C. Zwyssig, M. Duerr, D. Hassler, J.W. Kolar

Power Electronic Systems Laboratory

ETH Zurich

8092 Zurich, Switzerland

zwyssig@lem.ee.ethz.ch

Abstract— **New emerging micro gas turbine generator sets and turbocompressor systems push the speed limits of rotating machinery. To directly connect to these applications, ultra-high-speed electrical drive systems are needed. Therefore a 1 kW, 500000 rpm machine and the according power and control electronics are designed and built. This paper includes design considerations for the mechanical and electromagnetic machine design. Furthermore, a voltage source inverter with an additional dc-dc converter is described, and sensorless rotor position detection and digital control is used to drive the machine. Finally, the hardware and experimental results are presented.**

I. INTRODUCTION

The trend for air-compressors and miniature gas turbine generator sets is towards smaller power ratings and with the scaling of turbomachinery therefore towards higher speeds [1]–[4]. The definition of super-high-speed electrical machines is dependent on the required power level and the rated speed of the machine. Figure 1 shows the dividing line between high-speed and super-high-speed electrical machines as defined by [1] and the application areas for turbomachinery such as industrial and micro gas turbines and compressors. Extrapolating the turbomachinery line (dotted) predicts the operating range for ultra-high-speed drive systems as having speeds from 300000 to 1 million rpm and power levels between 10 W and 3 kW.

For the industrial gas turbines in the MW power range the grid-connected generator is coupled to the turbine through a gearbox and operates at a lower speed. Micro gas turbines with tens of kW of power that have direct connected high-speed permanent magnet (PM) generators/starters delivering 10 to 100 kW are becoming more prevalent [2], for example, the Capstone micro gas turbine operates at 90000 rpm with a power output of 30 kW. Several international research groups are investigating ultra-micro gas turbines with power outputs up to a 100 W for use in portable power applications [3]. Only a few of these projects consider the electrical system, although the electrical drive system is an integral part of the total system in order to start and generate electrical power from the turbines. For compressor systems the power and speed trends are similar to the turbines. One application is a fuel cell air compressor that requires 120000 rpm at 12 kW [5] and another is a 70000 rpm, 131 kW turbo compressor connected to a PM machine and an inverter [6]. Future automotive fuel cells will require low-power compressors which are small and lightweight and directly driven by high-speed electrical drives. All these emerging applications require an ultra-high-speed electrical drive system. Therefore, this paper presents a new machine and power electronics interface that is capable of
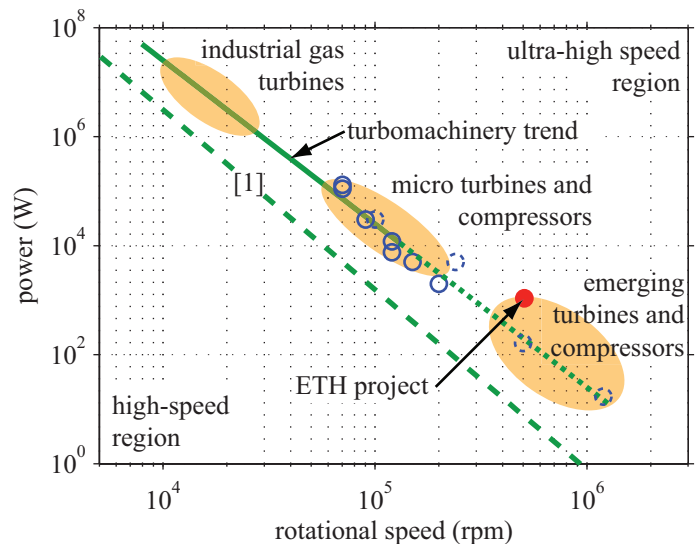

Fig. 1: Power and speed ratings of turbines and compressors and the trend line towards smaller power and higher speed. Systems referenced are plotted with circles, while future trends and planned systems are given as dashed circles. The ultra-high-speed electrical drive system is highlighted.

operating at 500000 rpm with a power output of 1 kW (see Figure 1).

The complete drive system is basically composed of three main parts as indicated in Figure 2. First, there is the electromechanical part, the permanent-magnet synchronous machine. The main challenges are the mechanical rotor design and the machine loss minimization. Further, the machine has to be supplied with currents of 8.3 kHz fundamental frequency by the power electronics. The drive system should run from a dc-voltage bus, and bi-directional power capability is needed. And last but not least the power electronics converter is driven by the control system, which includes sensorless rotor position detection and a cascaded torque and speed controller.

These main parts of the system are described in this paper and an experimental setup and measurements are presented. Section II describes the mechanical and electromagnetic machine design and presents the loss analysis. Section III covers the power electronic topology including the selection of the power semiconductors and the dimensioning of the passive components. Section IV deals with the control system including the common torque and speed control cascade, the sensorless rotor position detection and the realization on a
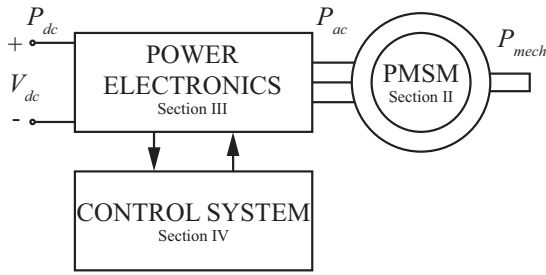
Fig. 2: Overview of the drive system, the input power P_{dc}, inverter output power P_{ac} and mechanical output power P_{mech} for motor operation.
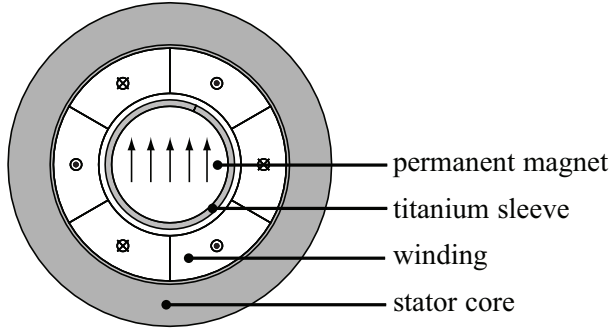

Fig. 3: Slotless, three-phase, permanent-magnet machine topology.

Fig. 4: Mechanical stresses in radial (σ_r) and azimuthal (σ_θ) direction in the rotor at 500000 rpm. The highest stress occurs on the inner side of the titanium sleeve in tangential direction, the most critical stress occurs in the middle of the permanent magnet due to its brittleness and therefore sensitivity to tensile stresses.

digital signal processor (DSP). Finally, Section V presents the hardware and experimental results.

II. MACHINE

The radial permanent-magnet machine with a slotless stator is found to be the best choice for ultra-high-speed operation, high power density and low high-frequency losses. [7], [4]. A previous design of a 100 W machine is adapted for the rated power of 1 kW, a rated speed of 330000 rpm and a maximum speed of 500000 rpm. The cross section of the machine is illustrated in Figure 3. The rotor consists of a cylindrical permanent magnet encased in a titanium sleeve and the cup-shaped air-gap winding is placed between the rotor and the slotless stator core.

A. Mechanical Design

The rotor diameter is limited by the mechanical stresses resulting from the high-speed operation. Especially the permanent magnet is sensitive to tensile stresses; therefore, it is shrink-fitted into a retaining titanium sleeve as shown in Figure 3. A permanent magnet diameter of 9 mm and a sleeve diameter of 10 mm is selected and the interference fit is 30 μm. The radial (σ_r) and azimuthal stresses (σ_θ) in magnet and sleeve are calculated according to the rotating disk theory in [8] and compared to the strengths of the materials. At maximum speed, the maximum stress in the magnet is 180 N/mm², which is on the limit of the tensile strength of the material. In the titanium, the maximum stress occurs on the inner side of the sleeve with 450 N/mm², which is a safety margin of two to the tensile strength. The stress distribution in the entire rotor at maximum speed is depicted in Figure 4.

Both bearing technology and rotor dynamics are depending on the application. Therefore, an analysis of bearings and bending modes is not included in this paper. As an example,
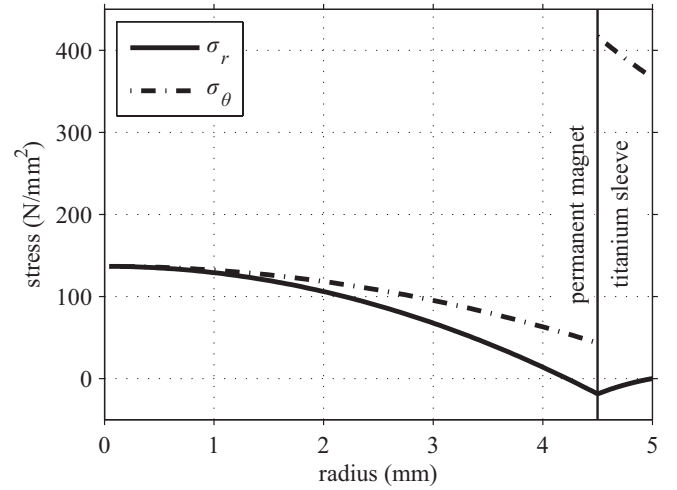
for a test bench the rotor dynamics and bearing technologies are analyzed in [7].

B. Electromagnetic Design

The electromagnetic design of the machine is carried out with the finite element software FEMAG, with the goal of a machine with a peak phase-to-phase voltage of slightly below 400 V (see Section III) and a rated torque of 19.1 mNm. The ironless rotor and the air-gap winding lead to a very low phase inductance of 43 μH (0.054 p.u.). A simulation of the phase back EMF, the impressed phase current (see Section III) and the resulting torque of the machine are shown in Figure 5 for rated power and maximum speed.

Iron-based amorphous metal (Metglas Magnetic Alloy 2605SA1) is used for the stator core in order to minimize the core losses. Furthermore, a Litz wire with 38 x 0.071 mm strands is used in order to minimize the eddy current losses. The air-gap winding is realized in Faulhaber design [11], with 42 turns per phase. In Table I, the geometrical data as well as the electrical specifications of the machine are summarized.

C. Loss Analysis

There are three main contributors to the total losses: copper losses, iron losses in the stator core and, in contrary to low-speed machines a big contributor, air friction losses in the air-gap.

The air friction losses $P_{f,air}$ can be analytically calculated according to [9]. With a friction coefficient c_f based on experimental data, the losses are calculated with

$$P_{f,air} = c_f \pi \rho_{air} \omega^3 r^4 l \qquad (1)$$

where ρ_{air} is the air density, r is the outer radius of the rotor sleeve and l the length of the machine. For the rated speed of 330000 rpm, (1) results in air friction losses of 18.8 W, and, due to the scaling with ω^3, they become 60 W at the maximum speed of 500000 rpm.
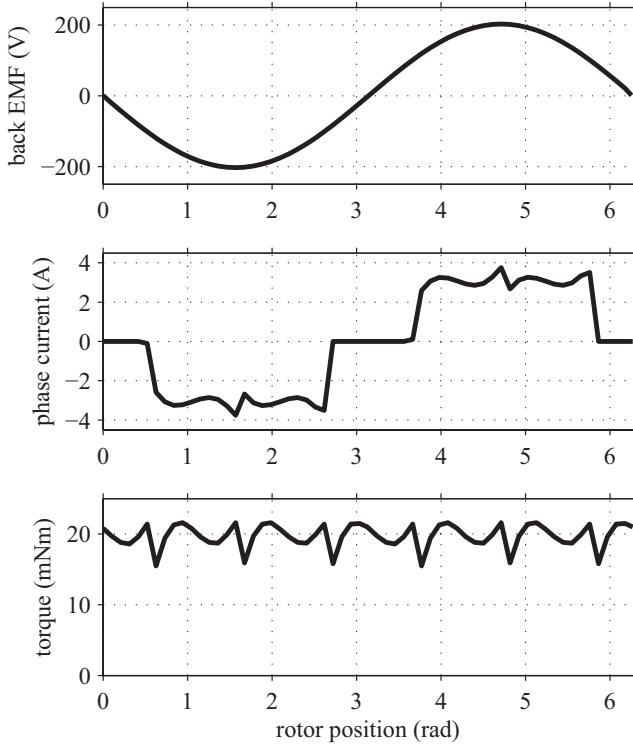
Fig. 5: Back EMF, impressed phase current and resulting torque of 19 mNm for a speed of 500000 rpm and a power of 1 kW.

TABLE I: machine data

geometry	
magnet diameter	9 mm
sleeve diameter	10 mm
interference fit	30 μm
stator core inner diameter	18 mm
stator core outer diameter	25 mm
active length l	30 mm
electrical data	
magnet flux linkage Ψ_{PM}	3.9 mVs
stator inductance L_s	43 μH
stator resistance R_s	0.5 Ω
nominal values	
connection	Y
number of pole pairs	1
rated current I_r	3.5 A
maximal speed n_{max}	500000 rpm
rated speed n_r	330000 rpm
rated power P_r	1 kW
rated torque T_r	19.1 mNm

The peak flux density $\hat{B}$ in the stator core is 0.8 T, and the frequency of the magnetic field for the two-pole machine is 5.5 kHz at rated speed and 8.3 kHz at maximum speed. With the Steinmetz law

$$P_{Fe} = C_m f^\alpha \hat{B}^\beta \qquad (2)$$

and the coefficients $C_m = 239$ W/m³, $\alpha = 0.82$ and $\beta = 0.32$ for amorphous iron, the iron losses can be estimated to 1.8 W for rated speed and 2.4 W for maximum speed, respectively.

The copper losses are calculated considering dc losses and eddy current losses due to the high frequency of the currents and the permanent magnetic flux penetrating the conductors in the air-gap winding. In order to minimize the high-frequency eddy current losses, a Litz-wire winding is used. According to [10], the losses can be calculated as the sum of dc plus skin-effect losses plus losses due to an external magnetic field $\hat{H}$

$$P_{Cu} = I^2 F + \hat{H}^2 G. \qquad (3)$$

The loss coefficients F and H depend on the diameter and number of the strands, the frequency and the geometry of the winding. At maximum speed and rated power, the copper losses are 9.2 W. At rated speed and power, they are slightly higher due to the higher torque (and therefore higher current) with 14.5 W.

Due to the low influence of the current on the magnetic field, the rotor losses can be omitted, although the inverter produces phase currents with a high harmonic content. The losses for the two operating points $P_{ac} = 1$ kW at 500000 rpm and $P_{ac} = 1$ kW at 330000 rpm are plotted in Figure 7 together with the power electronic converter losses.

III. POWER ELECTRONICS

In order to drive the machine with a PWM inverter, a very high switching frequency (above 200 kHz) and a high-bandwidth current control loop is needed. However, the high control dynamics that can be achieved with a PWM inverter are not needed for the mentioned applications. In [12], different converter topologies are compared regarding number of semiconductor devices, size of passive components, control complexity, and ease of sensorless operation.

In the literature, the chosen inverter topology and commutation strategy is referred to as variable dc link inverter [13], pulse amplitude modulation (PAM) inverter [14] or voltage source inverter (VSI) with block commutation [15]. It consists of a standard voltage source inverter topology and an additional dc-dc converter as shown in Figure 6. The inverter part is controlled in six-step or block commutation, which means that each switch is conducting for 120 electrical degrees and, therefore, switched with the fundamental frequency of the machine. The dc voltage $V_{dc,1}$ or the dc current I_{dc} can be controlled with the duty cycle of the dc-dc converter. For a sinusoidal back EMF and a low stator inductance as with the machine described in Section II, the resulting current waveform in one machine phase is shown in Figure 5. The topology has bi-directional power capability. Eight signals are needed to drive the gates of the transistors: two PWM signals for the dc-dc converter and six signals for the inverter. The dc current for the torque controller and the stator voltages for the sensorless rotor position detection and speed controller are measured and passed to the control system.

A. Electrical Dimensioning

The specifications for the power electronics are the input voltage ($V_{dc} = 400$ V), the maximum dc current for rated power and speed operation ($I_{dc} = 4.5$ A) and a maximum dc output voltage ripple of 5%. Free parameters are the dc-dc converter switching frequency and the values inductor L_{dc} and output capacitor $C_{dc,1}$.

The switching frequency is set to 100 kHz in order to keep the volume of the passive components low and realize a high-power density inverter. The trade-off between the sizes for capacitor and inductor leads to a small inductance and
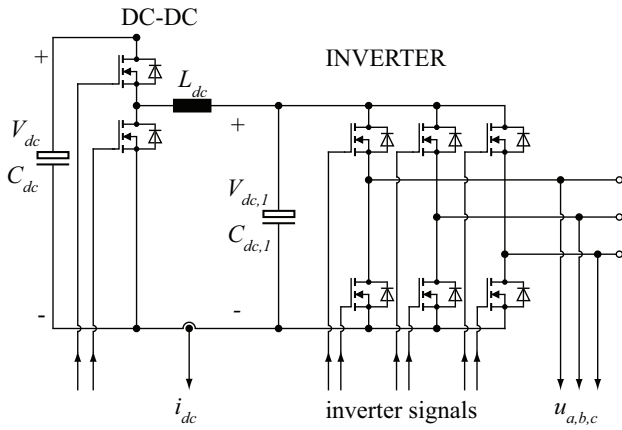
Fig. 6: Power electronics topology: VSI with additional dc-dc converter.

Fig. 7: Estimated power losses of inverter (at $115\,°C$) and machine for two different operating points ($P_{ac} = 1\,kW$ at 330000 rpm and $P_{ac} = 1\,kW$ at 500000 rpm).

therefore a big current ripple. In order to limit the losses in the inductor the maximum peak-to-peak current ripple (at the worst case duty cycle of 0.5) is set to 100% of the rated current. The values obtained are an inductance of $L_{dc} = 400\,\mu H$ realized with integrated SMD inductors (Coiltronics DR127-150) and a capacitance of $C_{dc,1} = 1320\,nF$ realized with multi-layer ceramic capacitors. The power-MOSFETs (IXYS IXFR 30N60P) are selected with respect to a low on-resistance $R_{ds,on}$ for low conduction losses and with a low reverse recovery charge Q_{rr} of the body diode for low switching losses.

B. Loss Analysis and Thermal Dimensioning

The losses in the power semiconductors can be divided into switching and conduction losses of the dc-dc converter ($P_{s,dc}$ and $P_{c,dc}$) and the inverter ($P_{s,inv}$ and $P_{c,inv}$). There are further losses in the inductors (P_L), and the losses in the ceramic capacitors can be neglected due to the low ESR.

The biggest losses are due to hard switching of one of the transistors in the dc-dc converter, for motor operation they occur in the high-side, for generator operation in the low side transistor. These losses can be reduced by reducing the switching frequency. The switching losses in the inverter can be neglected, whereas the conduction losses in the inverter are twice as large as in the dc-dc converter. The inverter losses are analyzed for two operating points: rated speed and power ($P_{ac} = 1\,kW$ at 330000 rpm and a resulting dc current of 4.5 A) and maximum speed and rated power ($P_{ac} = 1\,kW$ at 500000 rpm and a resulting dc current of 3A). An overview of the estimated losses is presented in Figure 7.

The thermal design is carried out for a maximum junction temperature of $115\,°C$ for worst-case operation and the worst-case transistor in the dc-dc converter. This leads to a heat sink with active air cooling and a thermal resistance R_{th} of $0.4\,K/W$. In addition, the air intake of the fan is used for the cooling of the inductors.

IV. CONTROL SYSTEM

The main tasks of the control system are the commutation of the inverter switches depending on the rotor position, and the cascaded current and speed control loops. The control system also provides communication with an external interface setting the speed reference, for example a PC. The stator-flux zero-crossing detection of the sensorless control is realized
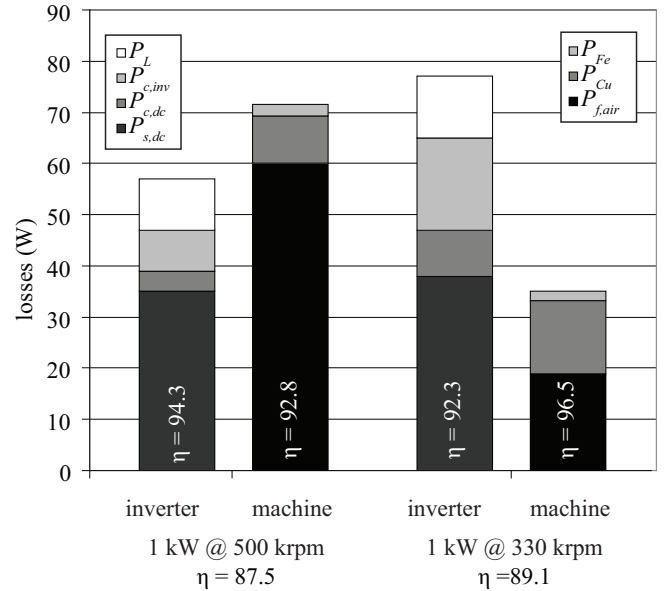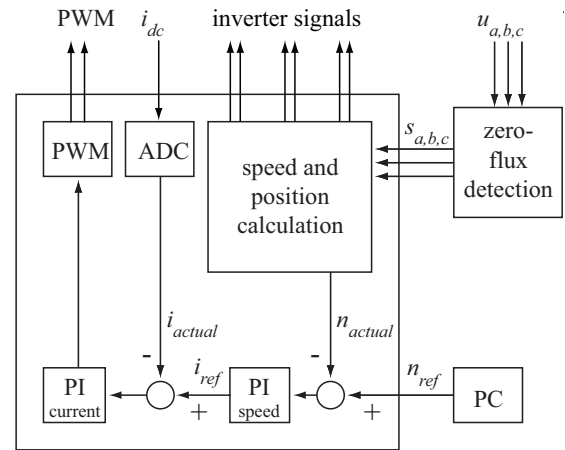

Fig. 8: Control system connecting to the power electronics.

with a discrete integrator and comparator circuit, whereas the rotor position and speed calculation is implemented on a digital signal processor (DSP), a Microchip dsPIC30F5016. Since all considered applications need only low dynamics of the speed control, simple torque control via the dc current is sufficient, which allows for a single, non-isolated shunt current measurement. The current reference is set by the speed controller. The entire control structure is presented in Figure 8.

A. Sensorless Control

A sensorless technique is used to control the stator currents, in order to overcome the disadvantages of rotor position sensors, such as an increased failure probability and an axial extension of the machine. Especially in ultra-high-speed machines, a longer rotor is unwanted because the critical speeds are lowered. Traditional sensorless control methods use model based estimation of the back EMF to calculate the rotor angle at any instant. The disadvantages are a large computation effort and the requirement of phase current measurements.

For an inverter with block commutation, the back EMF can be directly measured during the off intervals in each
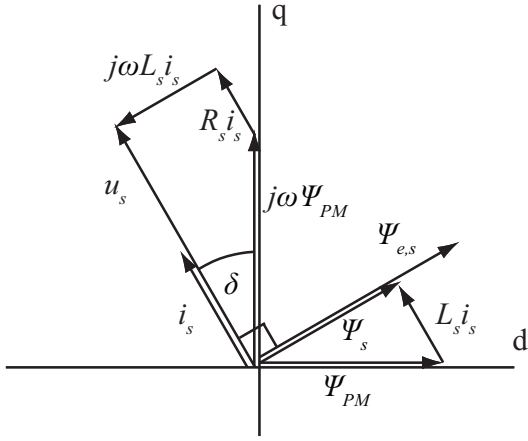
Fig. 9: Phasor diagram for the applied sensorless control (not drawn to scale). The stator current is controlled perpendicular to the stator flux.
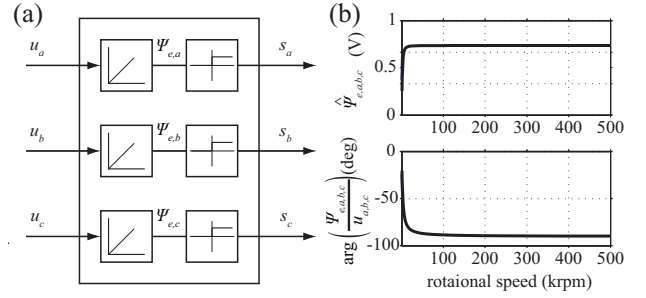

Fig. 10: Zero stator flux detection with integrators and comparators (a). The integrators are realized as first-order low-pass filters. Amplitudes of the signals before the comparator and phases difference of the signals before and after the integrator (b)

phase. The detected zero-crossings can be phase-shifted by 30 electrical degrees and used for switching operations, as described in [16] for brushless dc (BLDC) motors. The stator current is usually controlled approximately perpendicular to the permanent-magnet flux Ψ_{PM}, corresponding to maximum torque-per-current operation. Only digital signals are processed, and the computation effort is limited. Nevertheless, unwanted zero-crossings have to be digitally masked, and the 30-degree phase shift has to be implemented. The limited speed range due to the speed dependence of the back EMF amplitude and noise sensitivity are further drawbacks.

In the chosen solution, the currents are controlled perpendicular to the stator flux Ψ_s instead of the permanent-magnet flux as illustrated in Figure 9 for steady-state operation. The stator flux position is estimated by integrating the terminal voltages, leading to signals $\Psi_{e_{a,b,c}}$ in phase with the stator flux (Figure 10 a)). The detected zero-crossings of these signals are directly used for switching the inverter.

Since the stator currents are in phase with the stator voltages, the resistive voltage drop only influences the magnitudes of the signals $\Psi_{e_{a,b,c}}$ but not their phases. A comparison to the maximum torque per current operation can be made by considering the steady-state stator current displacement

$$\delta = \arcsin\left(\frac{L_s \hat{i}_s}{\hat{\Psi}_{PM}}\right) \qquad (4)$$

with respect to the back EMF induced by the permanent-magnet flux. The displacement is 3.1 electrical degrees for rated current, and results in a torque decrease of only 0.15%. The small influence of the stator current on the angle is due to the very low p.u. inductance of 0.055 for this machine (as typical for slotless machines), and thus low armature reaction. Further advantages are that, due to the integration, the terminal voltages are filtered and noise is reduced, the signals are phase shifted by -90 degrees and the zero-crossing of the signals happens at a commutation instant, and the integrated terminal voltages lead to signals with almost constant amplitudes. Similar sensorless techniques have been described in [17] for a BLDC motor and in [18] for a PM synchronous motor fed by a PWM inverter or a linear amplifier.

The integrator is realized in hardware as a first-order low-pass RC filter with a cross-over frequency of 45 Hz. A low

cross-over frequency is necessary to get a phase shift of -90 degrees at as low speeds as possible. The design of such a low-pass filter is a trade-off between having a phase shift of -90 degrees at low speeds and having a signal with a larger amplitude. Allowing a minimal phase shift of -80 degrees, the lower speed limit of the sensorless control is at 15000 rpm. The amplitudes and phases of the signals $\Psi_{e_{a,b,c}}$ are shown in Figure 10 (b).

After integration of the stator voltages, zero-crossing detection of the signals $\Psi_{e_{a,b,c}}$ with comparators leads to the digital signals $s_{a,b,c}$, which are inputs of the DSP, and the rotor position estimation and speed calculation then can be realized in software with a short computation time. The rotor position directly sets the state of the inverter, whereas the speed information is passed over to the speed controller. The starting of the machine can be achieved with impressed currents and a speed ramp.

V. EXPERIMENTAL ANALYSIS

A. Hardware

The volume of an electrical machine is mainly proportional to the torque. Therefore, the power density increases with speed, which leads to a very small machine for 1 kW output power. In contrary, power electronic converters have power densities depending on topology complexity, cooling and switching frequency. Furthermore, the control electronics volume is mainly depending on control complexity and component integration. With a volume of half a liter and a peak power of 2 kW the electronics are designed to have a power density of 4 kW/liter (65.5 W/in^3). A photograph of the machine parts (slotless stator core and Litz-wire winding, permanent magnet) and the electronics including power semiconductors, dc inductors, forced air cooling and heat sink, control electronics and auxiliary power supply can be found in Figure 11.

B. Measurements

In order to verify the analytical results of the power electronics design, efficiency measurements are carried out. Therefore a three phase resistive load is connected to the ac side in order to simulate the machine and the inverter is fed with 400 V dc voltage. For the two operating points described in Section III the measured losses are 36 W for 1 kW, 500000
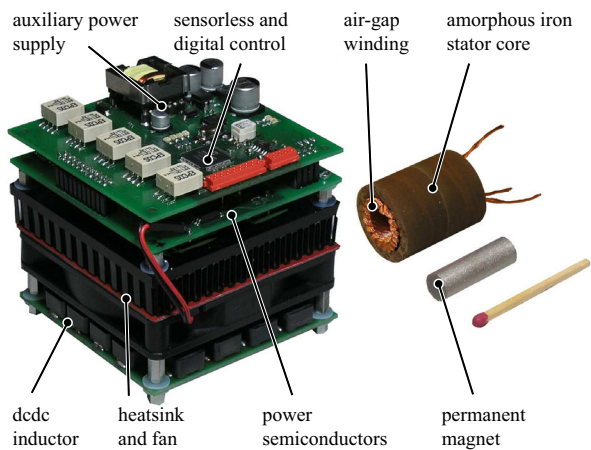
Fig. 11: Designed and built hardware: inverter including power semiconductors, dc inductors, forced air cooling and heat sink, control electronics and auxiliary power supply, machine stator and permanent magnet.
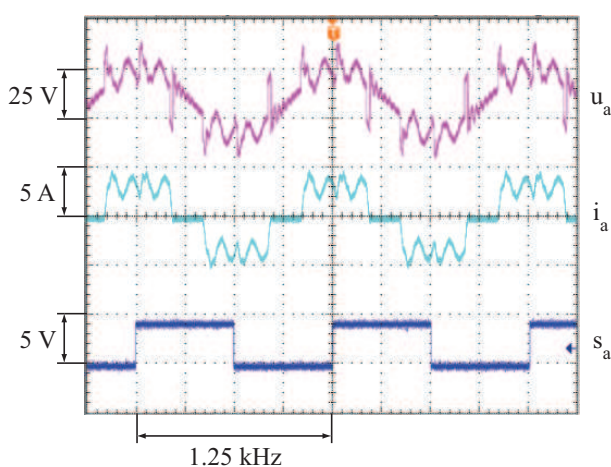

Fig. 12: Testing of the sensorless control at 75000 rpm and 3 A dc current. The zero-crossing signal s_a is phase shifted by -90 degrees to the stator phase voltage u_a.
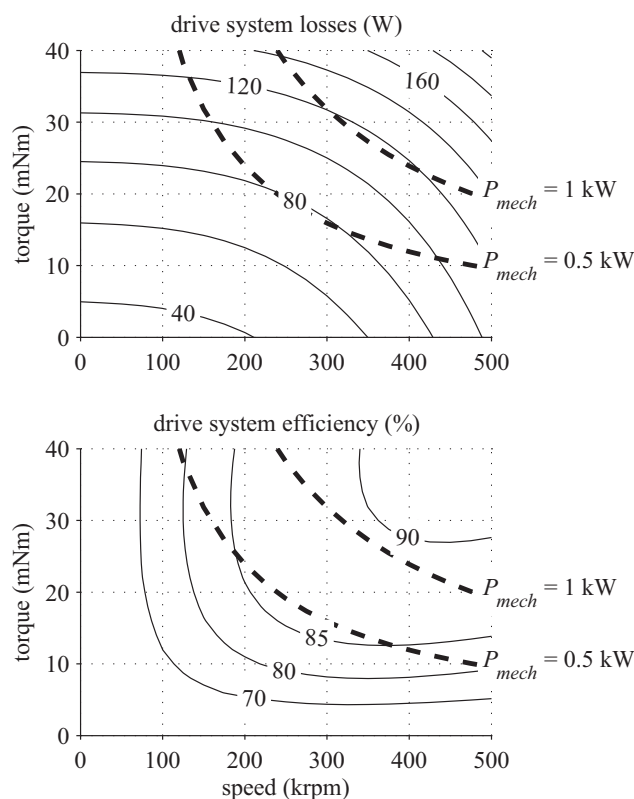

Fig. 13: Estimated losses and efficiency of the entire drive system in function of speed and torque. Two constant mechanical power lines are drawn for $P_{mech} = 1\,kW$ drive power and $P_{mech} = 0.5\,kW$.

rpm operation and 68 W for the 1 kW, 330000 rpm operation. The measured efficiencies are 96.5% and 93.6% respectively, which is slightly higher than calculated (Figure 7). The difference in measurement and calculation is due to worst-case considerations for the reverse recovery charge and the on-resistance of the MOSFETs.

The sensorless control is tested by connecting the inverter to a three-phase sinusoidal voltage source through inductors. For reduced speed and current operation of n = 75000 rpm and $I_{dc} = 3$ A the stator phase voltage u_a, the phase current i_a and the according sensorless signal s_a of one phase are shown in Figure 12. The stator phase voltage is distorted from the sinusoidal back EMF due to the phase current ripple and the resulting voltage in the phase inductor.

VI. CONCLUSION

New emerging applications require direct-drive, ultra-high-speed electrical drive systems. Therefore, a 1 kW, 500000 rpm machine and the according power and control electronics have been designed and built. The rotor diameter is limited by the acceptable mechanical stresses. The losses in the stator are minimized by choosing an appropriate high-frequency magnetic material, amorphous iron, and the use of Litz

wire. However, the main losses are due to air friction in the air-gap between rotor and stator. The power electronics topology is able to supply the machine with currents with the fundamental frequency of 8.3 kHz and allows for simple torque control via the dc current. The dimensioning and loss analysis leads to an compact inverter with a power density of $4\,kW/liter$ ($65.5\,W/in^3$). The implemented sensorless control method is feasible for ultra-high-speed operation and needs neither phase current measurements nor a large amount of computation time on the DSP. For characterizing the entire drive system the estimated power losses and the total efficiency are plotted in the speed-torque-plane (Figure 13).

The design of an ultra-high-speed drive system is an integrated task and the entire system including applications has to be considered when designing the single parts. The power electronics topology has to be chosen with respect to the machine, the low inductance is an advantage for the sensorless control. The block commutation strategy is chosen for low switching losses. The control can be simplified because no high-dynamics are needed for the intended applications.

REFERENCES

[1] M.A. Rahman, A. Chiba, and T. Fukao, "*Super high speed electrical machines - summary*," IEEE Power Engineering Society General Meeting, June 6-10, 2004, vol. 2, pp. 1272-1275.

[2] J. Oyama, T. Higuchi, T. Abe, K. Shigematm X. Yang, E. Matsuo, "*A trial production of small size ultra-high speed drive system*," IEMDC2003, vol. 1, no.2-1-1, pp. 31-36, 2003.

[3] S. A. Jacobson and A. H. Epstein, "*An informal survey of power MEMS*," ISMME2003, Tsuchiura, Japan, December 1-3, 2003, pp. 513-520.

[4] N. Bianchi, S. Bolognani, and F. Luise, "*Potentials and limits of high-speed pm motors*," IEEE Trans. Industry Applications, vol. 40, no. 6, pp. 1570-1578, Nov.-Dec. 2004.

[5] MiTi Developments (November 2005). Oil-free, motorized, automotive fuel cell air compressor/expander system [Online]. Available: http://www.miti.cc

[6] B. H. Bae, S. K. Sul, J. H. Kwon, and J. S. Byeon, "*Implementation of sensorless vector control for super-high-speed PMSM of turbocompressor*," IEEE Trans. Ind. Appl., vol. 39, no. 3, pp. 811-818, May-Jun. 2003.

[7] C. Zwyssig, J.W. Kolar, W. Thaler, M. Vohrer, "*Design of a 100 W, 500000 rpm permanent-magnet generator for mesoscale gas turbines*," IEEE Industry Applications Conference 2005, Conference Record of the 40th IAS Annual Meeting, Hong Kong, October 2-6, 2005, vol. 1, pp. 253-260.

[8] S. P. Timoshenko and J. N. Goodier, Theory of elasticity. McGraw-Hill Kogakusha, Ltd. 1970, ch. 4.

[9] C. Zwyssig, S.D. Round, and J.W. Kolar, "*Analytical and experimental investigation of a low torque, ultra-high speed drive system*," IEEE Industry Applications Conference 2006, Conference Record of the 41th IAS Annual Meeting, Tampa, FL, Oct. 8-12, 2006, Vol. 3, pp. 1507-1513.

[10] J. A. Ferreira, Electromagnetic modeling of power electronic converters. Norwell, Massachusetts: Kluwer Academic Publishers, 1989.

[11] F. Faulhaber. "Armature winding for rotary electrical machines," U.S. Patent 3 360 668, Dec. 26, 1967.

[12] C. Zwyssig, S.D. Round and J.W. Kolar, "*Power Electronics Interface for a 100 W, 500000 rpm Gas Turbine Portable Power Unit*," Applied Power Electronics Conference, Dallas, Texas, USA, March 19-23, 2006, pp. 283-289.

[13] K. H. Kim and M. J. Youn, "*Performance comparison of PWM inverter and variable DC link inverter schemes for high-speed sensorless control of BLDC motor*," Electronics Letters, Vol. 38, pp. 1294-1295, 2002.

[14] K. Taniguchi and A. Okumura, "*A PAM inverter system for vector control of induction motor*," Proc. IEEE PCC Conf., 1993, pp. 478-483.

[15] J. Zhang and M. Schroff, "*High-Performance Micromotor Control Systems*," The 29th Annual Conference of the IEEE Industrial Electronics Society, 2003. IECON '03, Volume: 1, 2-6, Nov. 2003, pp. 347-352.

[16] Z.Q. Zhu, J.D. Ede, D. Howe, "*Design criteria for brushless dc motors for high-speed sensorless operation*," International Journal of Applied Electromagnetics and Mechanics 15 (2001/2002) pp. 79-87 IOS Press.

[17] K. Iizuka, H. Uzuhashi, M. Kano, T. Endo, and K. Mohri, "*Microcomputer control for sensorless brushless motor*," IEEE Trans. Ind. Applicat., vol. IA-21, pp. 595-601, May/June 1985.

[18] J. Thur, "*Antriebssystem für höchste Geschwindigkeiten zur feldorientierten Regelung von permanenterregten Hochfrequenzspindeln ohne Drehgeber und ohne Signalrechner*," PhD dissertation, Bergische Universität Wuppertal, Germany, 2006.